Distribution Agreement

In presenting this thesis as a partial fulfillment of the requirements for a degree from Emory University, I hereby grant to Emory University and its agents the non-exclusive license to archive, make accessible, and display my thesis in whole or in part in all forms of media, now or hereafter now, including display on the World Wide Web. I understand that I may select some access restrictions as part of the online submission of this thesis. I retain all ownership rights to the copyright of the thesis. I also retain the right to use in future works (such as articles or books) all or part of this thesis.

Zacharia James Hadjri April 1, 2024

Correlated Phases and Dynamics of Excitons in van der Waals Heterostructures

by

Zacharia James Hadjri

Ajit Srivastava
Adviser

Department of Physics

Ajit Srivastava

Adviser

Luiz Santos

Committee Member

Lili Wang

Committee Member

2024

Correlated Phases and Dynamics of Excitons in van der Waals Heterostructures

By

Zacharia James Hadjri

Ajit Srivastava

Adviser

An abstract of
a thesis submitted to the Faculty of Emory College of Arts and Sciences
of Emory University in partial fulfillment
of the requirements of the degree of
Bachelor of Science with Honors

Department of Physics

2024

Abstract

Correlated Phases and Dynamics of Excitons in van der Waals Heterostructures

By Zacharia James Hadjri

Semiconducting transition metal dichalcogenides (TMDs) couple strongly to light via the excitation of electrons from the valence band to the conduction band, leaving a hole in the valence band. The excited electron binds to the hole forming an exciton, a hydrogenic quasiparticle. The interactions between excitons and between excitons and charge carriers can realize interesting phases of matter, especially in multi-layer stacks of TMDs. Heterostructures with type-II band structures can host interalyer excitons with a finite out-of-plane dipole moment. Furthermore, either a twist angle between layers or a large lattice mismatch can generate a moiré potential with a lattice constant orders of magnitude of larger than the underling lattices. This emergent long-wavelength potential is felt by both excitons and charge carriers.
In this thesis, we report firstly on the observation of electric-field tunable quadrupolar excitons in a WS2/WSe2/WS2 heterotrilayer and an interaction-driven quadrupolar-to-dipolar transition. Secondly, we describe the decay dynamics of interacting Moire excitons in a WS2/WSe2 heterobilayer where the exciton lifetime at short times increases with power up to hundreds of nanoseconds.

Correlated Phases and Dynamics of Excitons in van der Waals Heterostructures

By

Zacharia James Hadjri

Ajit Srivastava

Adviser

A thesis submitted to the Faculty of Emory College of Arts and Sciences
of Emory University in partial fulfillment
of the requirements of the degree of
Bachelor of Science with Honors

Department of Physics

2024

Acknowledgements

Firstly, I would like to thank my advisor Ajit Srivastava who has consistently guided me throughout my undergraduate career from my freshman year to my senior year and taught me how to be a good physicist. I must also thank my graduate student labmates Weijie Li and Luka Devenica, who helped me enormously in my development, as well as my fellow undergraduate Tony Li who worked with us for a semester and a summer.

I thank Prof. Luiz Santos for both serving on this committee and being a superb professor who taught me much about the theoretical side of our field, and for Prof. Lili Wang for being on my committee.

For the quadrupolar project, the DFT calculations were performed by Dr. Jin Zhang and Prof. Angel Rubio.

We thank Prof. Thomas Pohl, Dr. Jan Kumlin, and Dr. Lida Zhang from Aarhus University for theory work on cooperative decay dynamics and many insightful discussions.

The hBN crystals used were provided by Takashi Taniguchi and Kenji Watanbe at the NIMS group, and TMD flakes were provided by James Hone and Song Liu at Colombia University.

Table of Contents

List of Figures

Chapter 1

Introduction

The physical world is $3+1$-dimensional, meaning that there are three dimensions of space and one dimension of time. In the study of solid-state physics, most materials are similarly three-dimensional. However, in recent years it has been shown that it is possible, and surprisingly easy in fact, to isolate atomically thin crystals. Graphite, commonly known as pencil lead, is composed of sheets of carbon atoms weakly bound by van der Waals forces. Using Scotch tape, single layers can be isolated, making a quasi-two-dimensional crystal known as graphene. [1] Of course, this sheet of atoms is three-dimensional, but effectively, the concept of dimensionality depends on scales. For instance, if you look at a piece of string from a distance, it looks like a one-dimensional line. However, an ant on its surface would see two dimensions: one from walking along the string and another walking around its finite thickness. When we study solid-state physics, we are interested in the electrons in the solids, so the relevant length scale is the electron wavelength, which tends to be quite large in crystals since the electrons spread over the whole lattice. If the crystal is one atom thick, its thickness is much smaller than the electron wavelength, so for all intents and purposes, these electrons live in a $2+1$-dimensional spacetime. Other bulk materials can be similarly isolated into atomically thin sheets such as Transtion Metal Dichalcogenides

(TMDs). These materials are made of a unit cell containing one metal, such as Tungsten or Molybdenum, and two Chalcogens, such as Selenium, Sulfur, or Tellurium. These TMDs are of particular interest due to the fact that they couple strongly to light. [2, 3, 4]Furthermore, stacks of 2D materials can be built from these isolated sheets, which gives lots of freedom to design systems that might have interesting physics. [5] Twist angles between layers have also been of great interest due to their capability to create moiré potentials and enhance interactions. [6, 7, 8]

In this thesis, I will first give an introduction to our field, then I will present results on a quadrupole-to-dipole excitonic phase transition in a TMD heterotrilayer as well as results on using a bilayer as a platform for moiré-based cooperative quantum optics.

Chapter 2

Background

Semiconducting TMDs have been of great research interest recently, due to their two-dimensionality, strong spin-orbit coupling, and strong light-matter interactions, as well as their potential for creating superlattices out of them. Their chemical composition is MX_2, where M is a transition metal and X is a chalcogen. For this thesis, we will primarily be concerned with the TMDs WSe_2 and WS_2. They are both semiconductors. When they are monolayers, they have bandgaps of 1.7eV [9] and 2.05eV [10]. Additionally, the monolayer bandgaps are direct, meaning that the valence band maximum has the same wavevector as the conduction band minimum. Due to the direct bandgaps, an incident photon with sufficiently high energy can excite an electron from the valence band to the conduction band. The vacancy in the valence band after this excitation can be thought of as a positively charged quasiparticle known as an electron-hole or simply a hole. The hole in the valence band and the electron in the conduction band then attract and from a hydrogenic bound state, another quasiparticle known as an exciton. Let E_G be the bandgap, and E_B be the exciton binding energy. The minimum energy for an incident photon to excite an electron from the valence band to the conduction band is $E_G - E_B$.

The holes and electrons which comprise the exciton have finite wavefunction

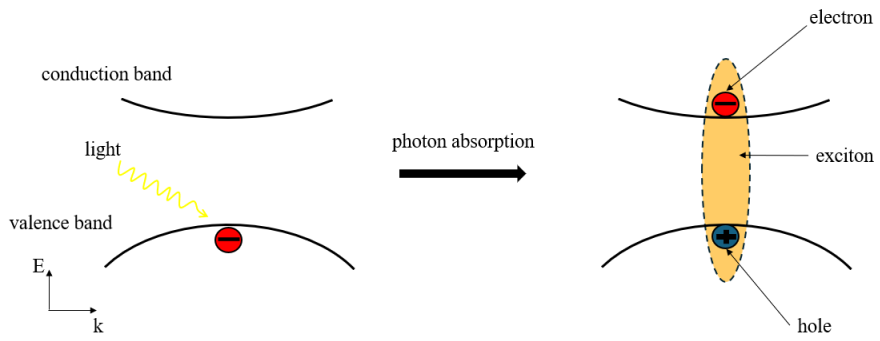

Figure 2.1: Light-induced exciton formation.

overlap, so with a characteristic lifetime, the electron will eventually relax back to the valence band, annihilating the hole and emitting a photon with energy $E_G - E_B$ in the process. This emission allows us to use photoluminescense (PL) spectroscopy as tool to probe these materials. Laser light shone on the sample of sufficiently high energy can populate many excitons into the system, and they will all emit light whose energy, and therefore wavelength, carries information about the binding energy of the exctions.

2.1 TMD vdW Superlattices

In their bulk form, the sheets of TMDs and other 2D materials are weakly bound to each other via van der Waals forces which scale as $\sim 1/r^7$. If monolayers are isolated, it is possible to manually construct stacks of different monolayers where the layers bind via the vdW forces to form bilayers, trilayers, and so on. For instance, a heterobilayer of two different TMDs, say WS_2 and WSe_2 could be made. Different TMDs have different band structures, so this freedom of assembling bilayers allows us to engineer the band structure of the composite system. There are three general band structure alignments of the composite system, as shown in Figure 2.2. The classification depends on the relative positions of the conduction band minima and the valence band maxima of the constituent layers.

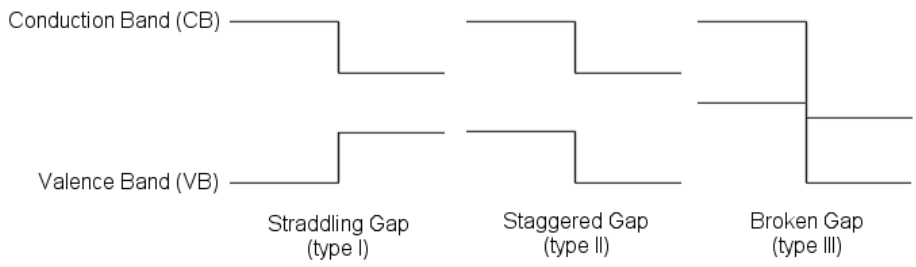

Figure 2.2: Heterojunction types

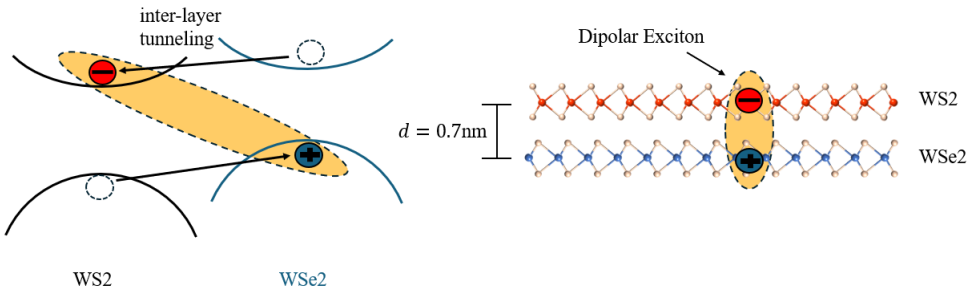

Figure 2.3: Type II Band Structure and Dipolar Excitons in WS_2/WSe_2

2.1.1 Dipolar interlayer excitons in heterobilayers

For excitons, the case of a type II band alignment is particularly interesting. Creating a heterobilayer of certain TMDs can produce a type II band structure, meaning that the conduction band minimum corresponds to one layer, but the valence band minimum corresponds to the other layer. Such is the case in a WS_2/WSe_2 heterobilayer. The electrons and holes can tunnel between layers, than such a band structure has the important consequence that electrons will tunnel to the layer with the lower conduction band minimum, and the holes will tunnel to the layer with the higher valence band maximum, i.e. the electrons and holes will occupy different layers. This interlayer separation applies to the optically doped carriers which comprise excitons, meaning that the electron and hole of the exciton will live in different layers. Such an exciton is known as an interlayer exciton (IX). A cartoon of this situation is shown in Figure 2.3. The layers have a separation of ~ 0.7nm, so this interlayer exciton has a finite out

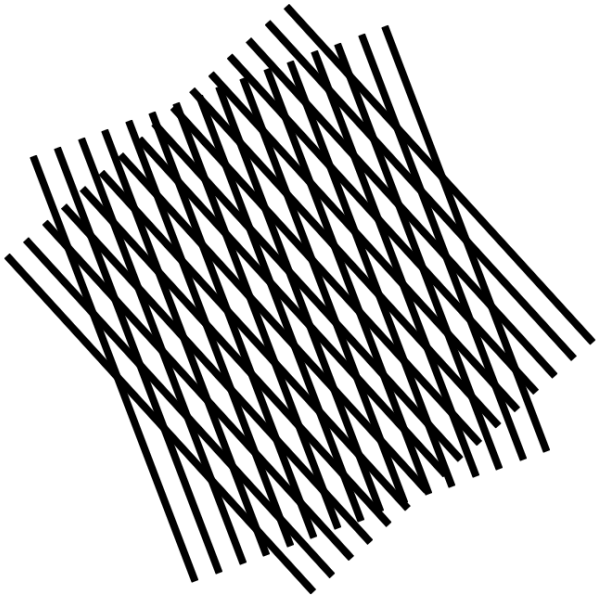

Figure 2.4: Simple moiré pattern from two sets of parallel lines with a relative twist.

of plane DC dipole moment. Thus, in an electric field its energy will shift linearly with the field strength. This change in exciton energy can be seen as a linear shift in the PL spectrum with electric field, as shown in Figure 4.2a. These dipolar excitons interact strongly which is of great importance since strongly interacting excitons can realize exotic quantum phases and phase transitions even in a driven-dissipative setting. [11, 12, 13, 14]

2.2 Moiré superlattices

Much of the interest in atomically thin materials is due to their capability of their heterostructures to form long-wavelength moiré potentials. The presence of moiré effects can have very interesting physical consequences, the shining example being the observation of superconductivity in Magic-angle twisted bilayer graphene. [15]. Moreover, in TMD heterostructures, Moiré potentials can cause the formation of Generalized Wigner Crsytal (GWC) states of electrons. [16, 17, 18]. The appearance

of a Moiré pattern is a very general phenomenon. For instance, taking two groups of equal spaced lines, twisting them relative to each other, and overlaying them creates a new pattern, shown in Figure 2.4. Importantly, the emergent pattern can have a much longer length scale than the underlying patterns.

In the case of 2D heterostructures, the underlying patterns are the atomic potentials of the constituent layers. Stacking two layers can create a new superlattice potential which can be much longer wavelength than the underlying lattices. In a homobilayer, such a long-wavelength moiré potential can be created by applying a small relative twist angle between the layers. However, a Moire potential can exist for a heterobilayer at zero twist angle if the two layers have a different lattice constant. The latter case occurs in WS_2/WSe_2 superlattices. The 4% lattice mismatch results in a Moire potential with lattice constant $a_M = 8$nm. [17]

Chapter 3

Methods

3.1 Exfoliation

For isolating monolayers of TMDs such as WS_2 and WSe_2, bulk crystals were placed onto scotch tape. The tapes were then placed onto 300nm Si/SiO_2 substrates and heated at 100°C for 3 minutes. The tapes were then pulled off of the silicon substrates, and the substrates were searched for monolayer flakes of the TMDs using an optical microscope. When a potential monolayer was found, it was verified by checking that it showed room-temperature photoluminescence by applying optical filters to the microscope which allow short-wavelength light onto the sample but only allow the long-wavelength light emitted by the sample to be seen.

For the hBN and graphite flakes used in the devices, an identical exfoliation procedure was used with their bulk crystals. However, we did not search for monolayers but for layers of thickness of nanometers to tens of nanometers.

3.2 Sample assembly

To create dual-gated heterostructure devices, we used the standard PC-based dry-transfer technique. [19] Firstly, electrodes were patterned onto 300nm Si/SiO_2 sub-

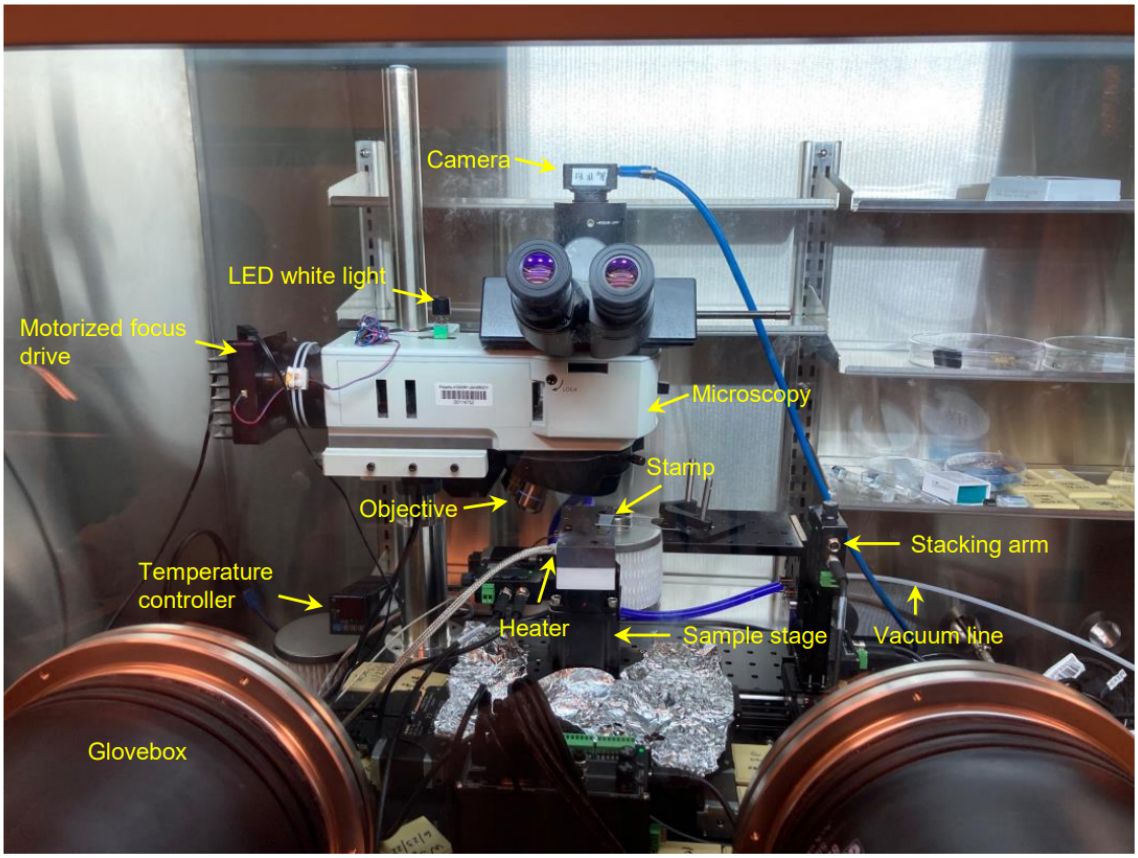

Figure 3.1: Glovebox containing dry-transfer pickup setup.

strates using EBL and then 5nm Cr/85nm Au was deposited using thermal evaporation. Then, after designing a device using CAD software, the stack of graphite, hBN, and TMDs was assembled by picking the flakes with a PC/PDMS-based stamp at a stage transfer of 60-80°C in a glovebox. The dry-transfer setup in the glovebox is shown in Figure 3.1. The stage can be rotated to align flakes and create twist angles between flakes. The stack was then placed onto the electrodes, and the PC was detached along with the sample by increasing the stage temperature to 150-180°C.

3.3 Optical measurements

Optical measurements were performed using two different 4K cryostats. One is an AttoDry 800 closed-cycle cryostat. Samples are mounted on piezoelectric nanopositioners

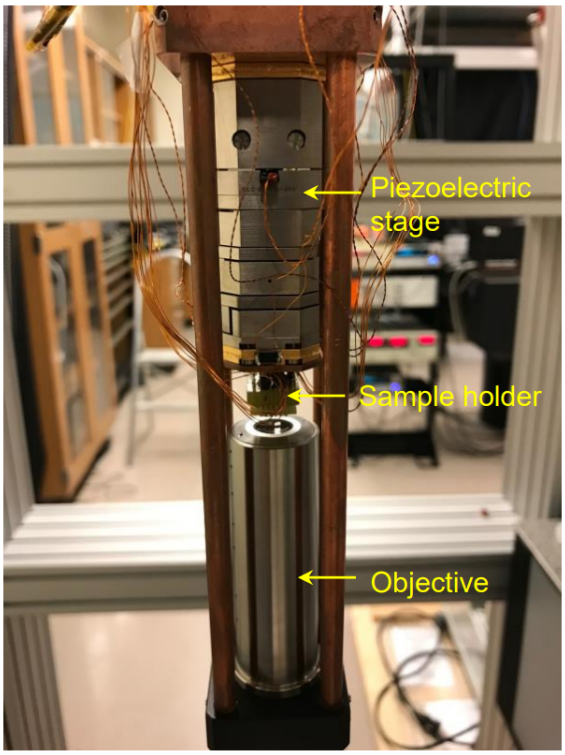

Figure 3.2: Nanopositioners, sample holder, and objective in BlueFors cryostat setup.

from Attocube systems, and we use an objective lens with NA= 0.42 to collect the near-infrared emission from the samples. The light is then analyzed with 500mm-focal length Princeton Instrument HR- 500 spectrometer with a 300g/mm grating. The PL is detected on a thermoelectically-cooled Princeton Instrument PIXIS-400 CCD.

The other setup is a Bluefors closed-cycle cryostat with an 8T magnet. This setup also uses Attocube nanopositioners to move the sample, and has an objective lens with NA= 0.63 to collect emission light. Its spectrometer is a Princeton Instruments SP-2750 with 300g/mm grating and a liquid nitrogen-cooled PyLoN CCD.

Continuous-wave PL measurements were performed using a MSquared tunable CW Ti:Sapphire laser. The spot size of this laser is $\sim 1\mu$m. The incident laser light can be ciruclarly polarized using a polarizer and a $\lambda/4$ waveplate. Co- and cross-polarized emission can be selected by a using another $\lambda/4$ waveplate and a polarizer after the objective.

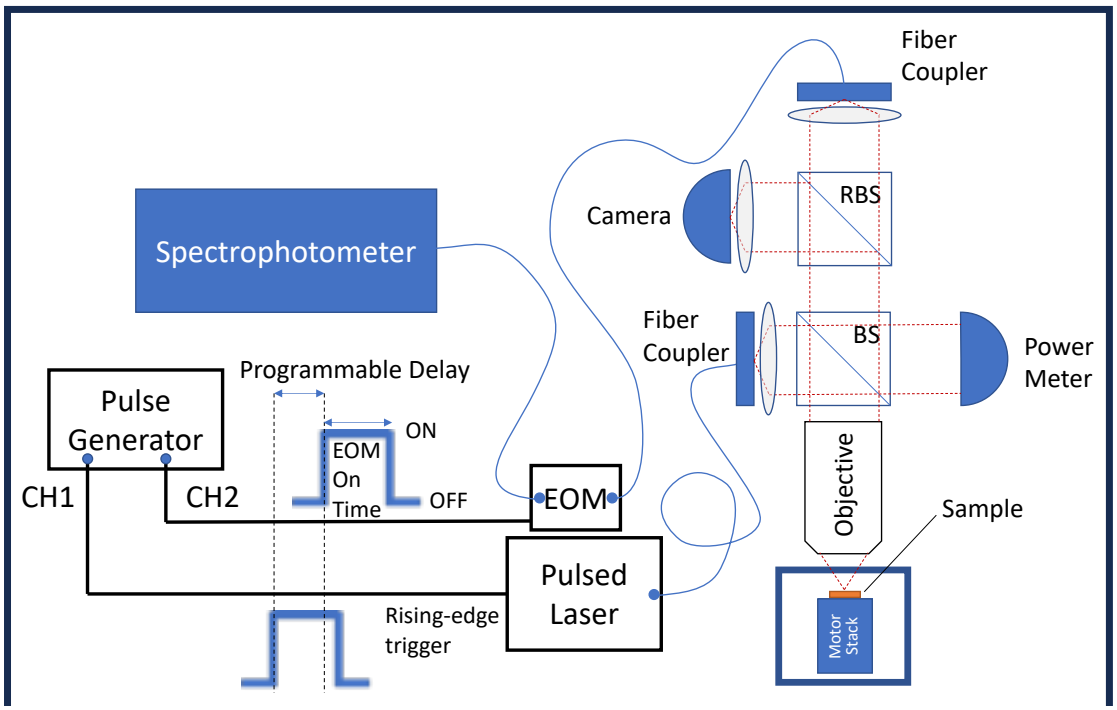

Figure 3.3: Schematic of the setup used to take time-resolved PL spectra.

3.3.1 Time-resolved PL measurements

For lifetime measurements, a pulsed 640 nm laser was used. The pulse frequency is tunable from 1 to 80 MHz. A pulse excites many excitons within the sample, which eventually decay. Using an avalanche photodiode (APD), the time between the pulse and a photon being emitted can be measured. Thus, we can easily measure the emission intensity as a function of time elapsed since an initial laser pulse. Filters were used to select certain wavelength regions of interest when necessary.

For time-resolved PL spectroscopy, an RF pulse generator was used with an AeroDIODE fiber-coupled acousto-optic modulator (AOM). The AOM can either block or let through the light in the fiber at RF frequencies. Using the pulse generator and the pulsed laser's output signal, square-waves with 20ns width were generated with a controllable delay relative to the laser pulse. These pulses are shown diagramatically in Figure 3.3. The AOM used this square-wave output on CH2 as an input and only allowed light to pass through for this 20ns interval at a programmable delay. The PL

emission from our standard setup discussed above was plugged into the AOM with a fiber-optic cable, and the AOM's output fiber was collimated and then measured by the spectrophotometer.

Chapter 4

Quadrupolar Excitons in a WSe_2/WS_2 Heterobilayer

This chapter shows our discovery of quadrupolar excitons in a TMD hetrobilayer, and evidence for a density-driven quadrupolar-to-dipolar phase transition. There have previously been several reports on the hybridization of inter- and intralayer excitons in bilayers, but they still had dipolar character. [20, 21, 22] This content is also the subject of our group's paper titled 'Quadrupolar-dipolar excitonic transtion in a tunnel-coupled van der Waals heterotrilayer.' [23] Similar results on quadrupolar excitons were also reported by other groups around the same time. [24, 25, 26]

4.1 Experimental Details

The sample was constructed using a standard dry-transfer technique and placed on a silicon substrate with gold electrodes, as described in the methods section. A tear-and-stack method was used for the bottom and top WS_2 layers, meaning that a single WS_2 monolayer was torn using the dry-transfer setup to create the outer layers. This tearing ensures that relative twist angle between the outer layers is near zero. The sample is encapsulated in bulk hBN to create a high-quality dielectric

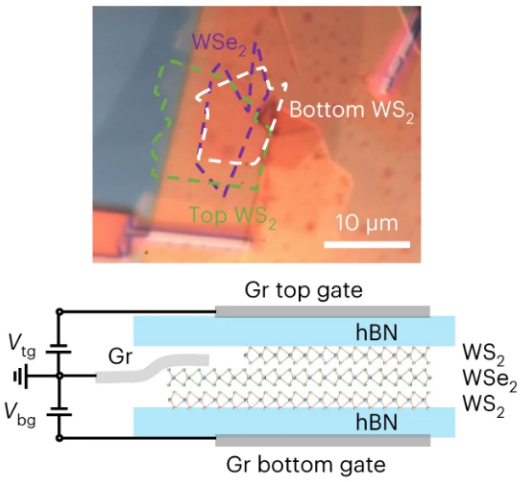

Figure 4.1: **a.** Optical image of the dual-gated sample with the TMD monolayers outlined. Note that the sample contains a heterotrilayer region as well as heterobilayer regions. **b.** Cartoon of device schematic. The sample is encapsulated in hBN and dual gated. The TMDs are also grounded via a graphite contact.

environment, and is dual gated with graphite. A thin piece of graphite is also used as a contact to ground the TMDs. A cartoon of this structure is shown in Fig. 4.1. The electrodes are 5nm/95nm Cr/Au and are used to ground the contact and apply voltages to the gates. Since voltage can be applied to each gate independently, this design allows for complete control of the electric field between the gates as well as the chemical potential.

4.2 Evidence of Quadrupolar Excitons

Dipolar excitons in TMD heterobilayers can be observed via photoluminescence spectroscopy by observing their stark shift. [27] Applying an electric field by the gates causes the exciton energy to change linearly, so its PL emission energy will likewise shift linearly with electric field. In fact, this sample's bilayer region shows such dipolar excitons in its photoluminescence, as shown in Figure 4.2a. However, the PL in the trilayer region, shown in Figure 4.2b., shows markedly different qualitative behavior.

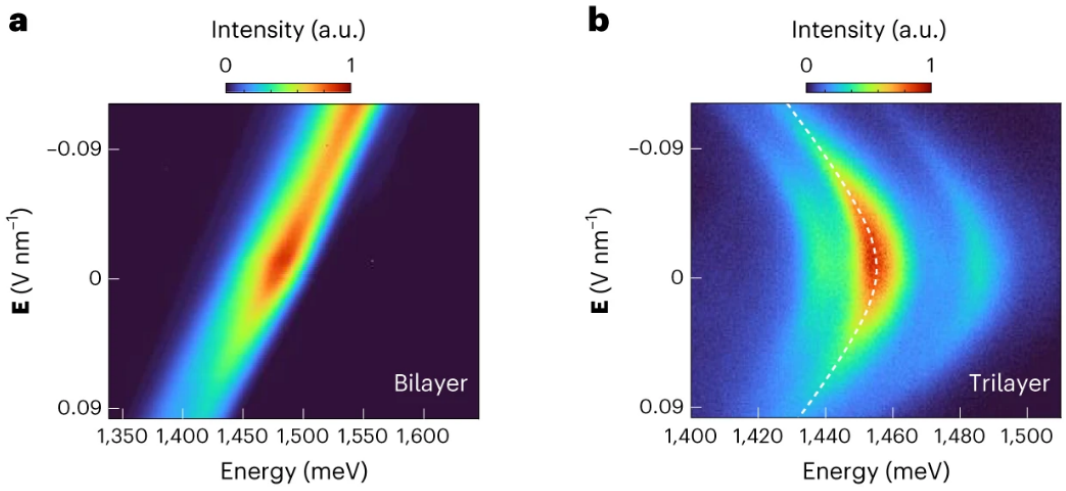

Figure 4.2: **a.** PL dependence of electric field for a WS_2/WSe_2 bilayer region within the heterotrilayer sample. **b.** Electric field dependent PL of the trilayer region.

Firstly, it has a three-peak structure, and, in order of decreasing energy, we attribute these peaks to a spin-triplet IX, a spin-singlet IX, and the singlet's phonon replica, based on previous results of WS_2/WSe_2 bilayers. [28, 29] In stark contrast to the bilayer PL, the photoluminescence only redshifts with electric field. Furthermore, it has a 'C'-shaped curve reminiscent of a hyperbola. We attribute this energy dispersion with electric field to the presence of quadrupolar excitons. In the trilayer region, there could be both up dipoles, with a hole in the middle WSe_2 layer and an electron in the top WS_2 layer, and down dipoles with the electron in the bottom WS_2 layer. Because the electrons can tunnel between the outer layers, in general we expect that the excitons form a superposition of up and down dipoles. This situation is shown as a cartoon in Figure 4.3a. Both a symmetric and anti-symmetric superposition of dipoles is possible. DFT calculations were performed for the trilayer system, and it was found that for the symmetric superposition, the hole predominantly has weight in the outer layers, but has small weight in the middle layer (Figure 4.3b.). However, the anti-symmetric superposition has no weight in the middle layer (Figure 4.3c.).

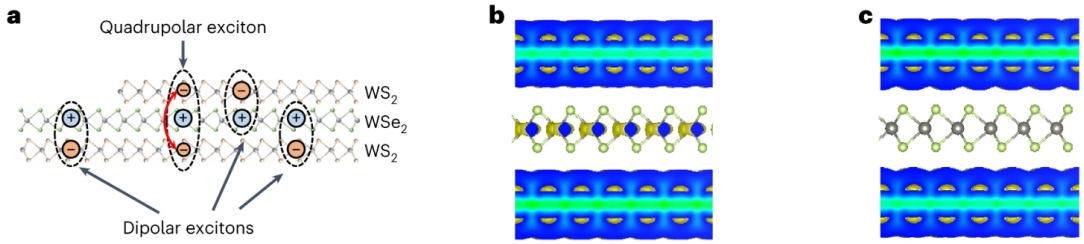

Figure 4.3: **a.** Cartoon of dipolar and quadrupolar excitons in heterotrilayer. **b.** Orbitals of symmetric quadrupole obtained from DFT calculations. Note that there is finite weight in the middle WSe_2 layer. **c.** Orbitals of anti-symmetric quadrupole. There is no weight in the middle layer.

4.2.1 Model

The 'C'-shaped PL found in the trilayer region can be explained with a simple model. If we consider a two-dimensional Hilbert space spanned by $|\mathbf{up}\rangle$ and $|\mathbf{down}\rangle$, referring to the states of an up and down dipole, respectively, then the Hamiltonian can be written as

$$\mathcal{H} = \begin{pmatrix} +\alpha\mathbf{E}\cdot\mathbf{d} & -t_0 \\ -t_0 & -\alpha\mathbf{E}\cdot\mathbf{d} \end{pmatrix}, \tag{4.1}$$

where $\mathbf{E}$ is the electric field, $\mathbf{d}$ is the dipole moment of an exciton, α is a parameter to account for screening, and t_0 is a hybridization energy. Its eigenvalues are

$$\mathcal{E}_{\pm}(\mathbf{E}) \pm \sqrt{t_0^2 + \alpha^2(\mathbf{E}\cdot\mathbf{d})^2}. \tag{4.2}$$

These energies clearly depend on the applied electric field, and when plotted, form hyperbolae as shown in Figure 4.4a. The lower-energy branch aligns nicely with the trilayer PL, including its linear behavior at high electric fields.

However, a more accurate description of the quadrupole's dependence on electric fields should consider how the symmetric wavefunction evolves. In Figures 4.4c. and d., DFT calculations of the electron charge density are shown for $\mathbf{E} = 0.015$V/nm and $\mathbf{E} = 0.03$V/nm in c. and d., respectively. We see that at higher electric field,

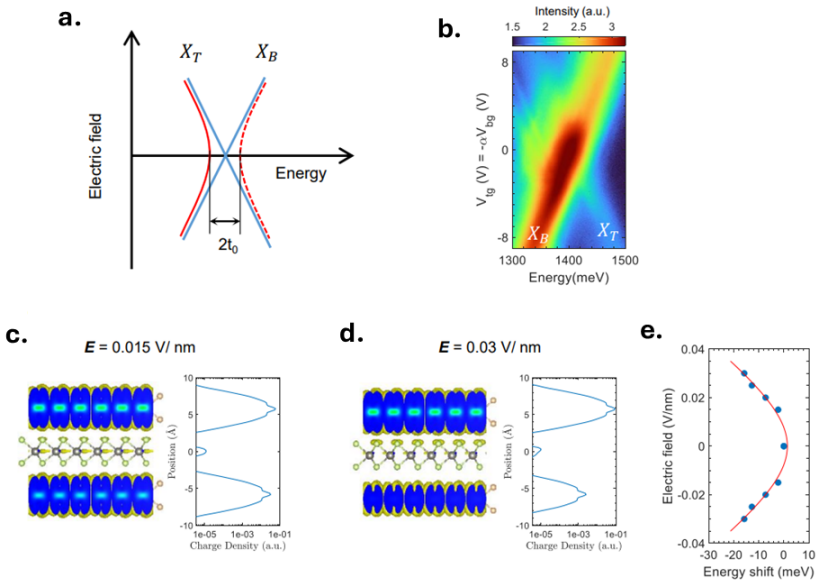

Figure 4.4: **a.** Hybridization of the top and bottom dipoles. X_B (X_T) is the bottom (top) dipole and t_0 is the tunnelling strength at zero electric field. The solid red line is the lower energy symmetric branch, and the dashed red line is the higher energy anti-symmetric branch. **b.** **E**-dependent PL of an AB stacked trilayer. The top and bottom dipoles do not hybridize. The excitation power is 5μW with energy 1.685 eV. **c, d.** DFT calculation of the electron charge density across the layers at $\mathbf{E} = 0.026$V/nm (c) and $\mathbf{E} = 0.05$V/nm (d). When **E** is increased, the electron density is shifted from the bottom layer to the top layer, and the electron density in the middle layer is reduced. **e.** The solid blue dots represent the shifts of the quadrupolar exciton interband transition energy as a function of **E** from DFT calculations. The red line shows the hyperbolic fit of Figure 4.2b.

the charge density shifts to the upper layer as expected, with the weights in both bottom layers decreasing. The loss of electron weight in the middle layer results in less electron-hole overlap, explaining the reduced PL intensity at higher electric fields. In Figure 4.4e., the blue dots are DFT calculations the interband transition energy as a function of electric field. The red curve is a hyperbolic fit of the quadrupolar PL in Figure 4.2b., with $t_0 = 16 \pm 5$meV. The fitting shows remarkably good agreement with the DFT calculations. The DFT calculations ignore the effects of the moiré potential, so this strong agreement of the data with the calculations suggest that moiré effects are not important in this system.

4.2.2 AB-stacked heterotrilayer

Tunneling of electrons between the outer two WS_2 layers is crucial for the dipolar excitons to hybridize and form quadrupolar excitons. Naively one would predict that if this tunnelling were forbidden, the PL dispersion would have an 'X' shape, like the blue asymptotic lines in Figure 4.4a. The sample with quadrupolar excitons used a tear-and-stack method to have near-zero twist angle between the two WS_2 layers, called 'AA' stacking, and with this twist angle interlayer tunneling is allowed. However, if the top WS_2 is twisted 60° relative to the bottom one, referred to as an 'AB' stacking, the interlayer tunneling is forbidden due to spin-valley conservation. [30] A heterotrilayer with such a 60° relative twist between the outer layers was constructed, and its PL as a function of electric field is shown in Figure 4.4b. Indeed, as expected, there is no hyperbolic shape indicative of quadrupolar excitons. Instead, there is an 'X' shape comprised of two linearly dispersing peaks which do not appear to mix with each other. We attribute these peaks to the two unhybridized types of dipoles present. The discrepancy in emission intensity due to the bottom dipole corresponding to an AA-stacked WS_2/WSe_2 bilayer and the top dipole corresponding to an AB-stacked heterobilayer. The latter's excitons have more momentum mismatch and therefore

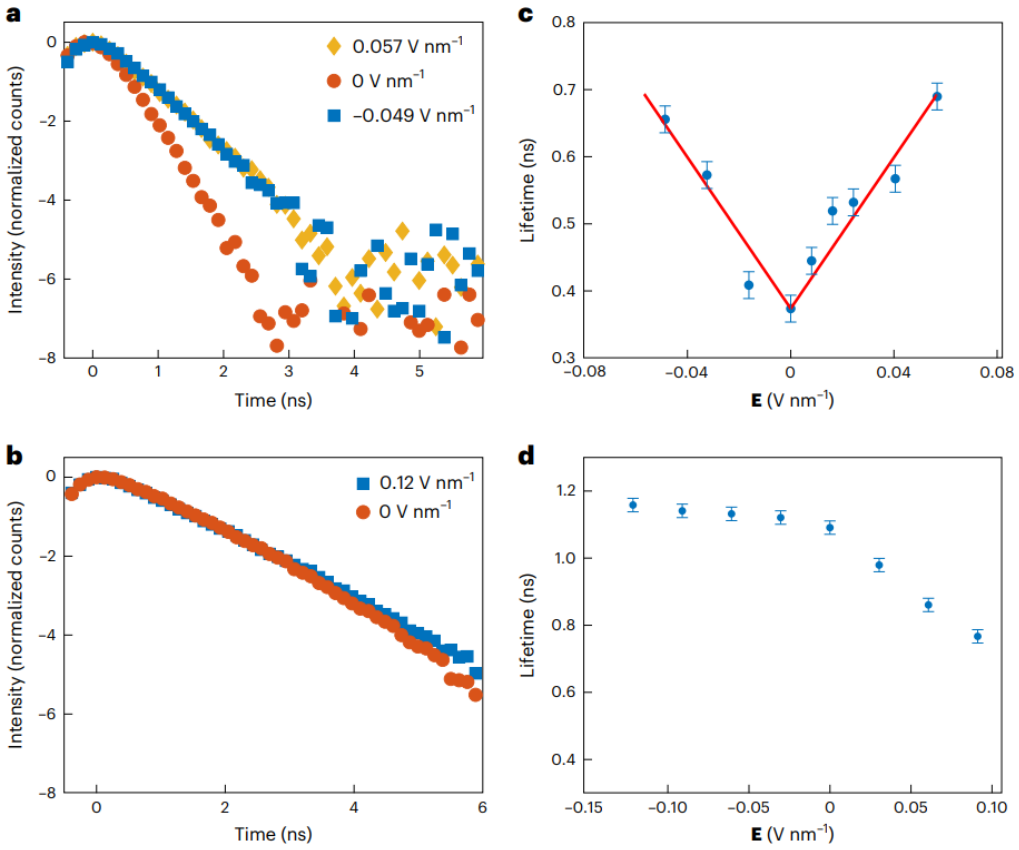

Figure 4.5: **a.** Time-resolved PL intensity measurements of the heterotrilayer region at electric fields of -0.049, 0, and 0.057V nm^{-1}, which are the blue squares, red dots, and yellow diamonds, respectively. **b.** Quadrupolar lifetime as a function of electric field. **c.** Time-resolved PL measurements of the heterobilayer region at electric fields of 0 and 0.12V nm^{-1}, which are the red dots and blue squares, respectively. **d.** Dipolar lifetime as a function of electric field.

have longer lifetime.

4.3 Control of excitonic lifetime with electric field

The lifetime of an exciton depends on the overlap of the electron wavefunction with that of the hole. Given that the symmetric quadrupole wavefunction in the middle layer and that the electron's weight shifts to the outer layers via the application of an external electric field, in principle the overlap can be tuned by electric fields. This allows for the electric field to be a knob which controls the oscillator strength and the

light-matter interactions of the excitons. Lifetime plots of the PL emission from the heterotrilayer region at selected electric fields are shown in Figure 4.5a. The lifetime is clearly higher at nonzero electric fields in either direction, as expected due to reduced electron-hole overlap. A plot of electric field as a function of electric field is shown in Figure 4.5c. No matter which direction the out-of-plane electric field is applied, the lifetime increases linearly from $\sim 0.4 - 0.7$ns with electric field, showing that the external field can control the emission intensity and light-matter interactions of these quadrupoles.

Lifetime plots at 0 and 0.12V nm^{-1} for the bilayer PL emission are shown in Figure 4.5b., and this dipolar lifetime as a function of time is shown in Figure 4.5d. In contrast to the quadrupolar excitons, the lifetime of the dipolar excitons shows negligible change for $\mathbf{E} < 0$ since the electron and hole wavefunctions are not highly tunable with electric field. For $\mathbf{E} > 0$, there is a reduction in lifetime which is also apparent in Figure 4.2a. This effect is likely due to non-radiative decay caused by accidental doping as the electric field is applied.

4.4 Interaction-driven quadrupolar-dipolar transition

Dipolar excitons in heterobilayers have a strong repulsive interaction [31, 32, 33]; however, quadrupolar excitons should interact much more weakly. However, this weak repulsion could still result in many interesting phases and transitions between them, including dipolar crystallization. [34] In another $WS_2/WSe_2/WS_2$ device, a similar electric field dependence of PL in the trilayer region was observed. Although there are some small qualitative differences in comparison to Figure 4.2b., the emission similarly only redshifts with electric field, suggesting that layer-hybidized quadrupolar excitons exist in this sample as well. The dispersion with electric field at 35μW of

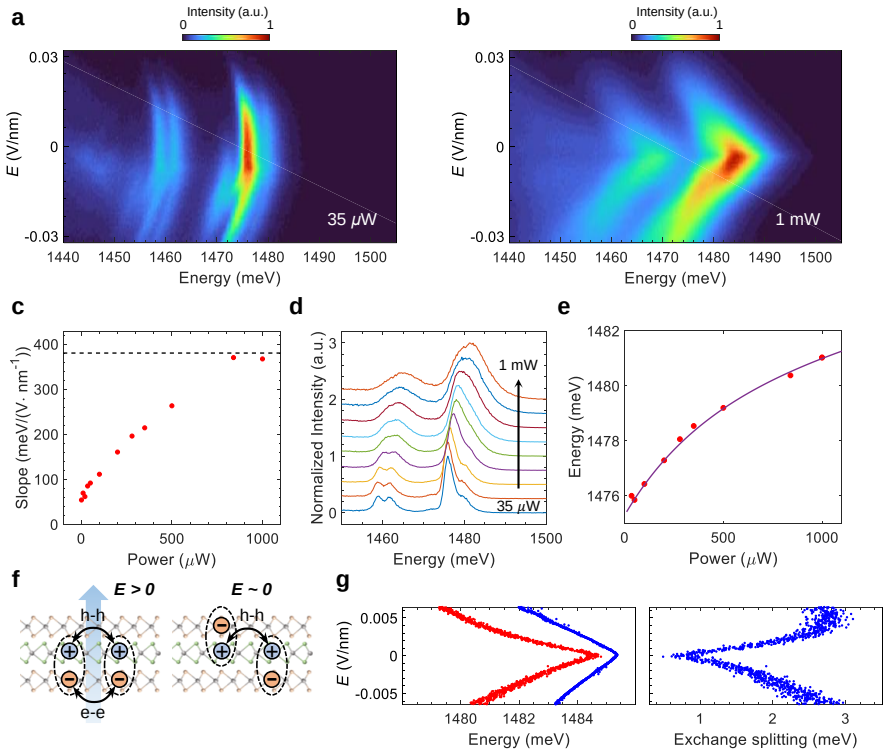

Figure 4.6: **a.** Electric field dependence of PL with a low excitation power of 35 μW. Peak energies have a hyperbolic dependence on the gate voltage. **b.** Electric field dependent PL with a high power of 1 mW. Peak energies have a linear dependence on the gate voltage. The laser excitation energy for both **(a)** and **(b)** is 1.696 eV. **c.** Fitted quadrupolar exciton energy shift slope of the top half branches as a function of incident power. The slope increases with the power. The dashed horizontal line is the asymptotic line slope of low power at high **E**. **d.** Normalized spectra from 8.4 mV/nm under excitation power of 35, 50, 100, 200, 280, 350, 500, 840, and 1000 μW. **e.** Extracted energies of the strongest peaks from panel **(d)**. The peak energies blue-shift under increased power. The peak energy error bar is $\pm$0.03 meV. The purple curve is a fit. **f.** Schematics of exchange interactions at $\mathbf{E} > 0$ and $\mathbf{E} \sim 0$. Both electron-electron and hole-hole exchange interactions exist for $\mathbf{E} > 0$ whereas only hole-hole exchange interactions exist for $\mathbf{E} \sim 0$. **g.** Zoomed-in electric field dependence of co- (blue dot) and cross-polarized (red dot) strongest peak energies (left) and their energy splitting (right) at 1 mW.

laser power in Figure 4.6a. appears to be hyperbolic like the other device. However, at 1mW, the PL is qualitatively different; it looks much more linear although it still only redshifts. This linear dispersion with electric field, as opposed to a 'C'-shape, is remniscent of dipolar excitons, possibly suggesting a transition from a quadrupolar phase to a dipolar phase as the incident laser power is increased.

In Figure 4.6c., a the top half of the PL emission was fit linearly for different excitation powers, giving an effective slope of the dispersion with electric field. This effective slope is proportional to the average dipole moment of the exciton. With power, this slope increases and then saturates near 1mW. Furthermore, the emission energy at the electric field of the 'turning point' blueshifts with power, as shown by the linecuts in Figure 4.6d, and the peak positions in Figure 4.6e. The qualitative change in the PL with power suggests that the quadrupoles are de-hybridizing as the density of quadrupoles increases. Quadrupoles weakly repel, but oppositely-aligned dipoles attract. at sufficiently high densities this repulsion could be large enough to overcome the hybridization energy. The blueshift with power of the turning point could suggest that this de-hybridization is indeed taking place.

4.5 Exchange splitting and signatures of anti-ferroelectric correlations

When the trilayer region is excited with circularly polarized light, the co-polarized emission has different energy than cross-polarized emission, suggesting the presence of strong exchange interactions in the system. The left panel of Figure 4.6g. shows the strongest peak energies for co-polarized emission (blue) and cross-polarized emission (red) at 1mW of excitation power for small electric fields. The right panel shows the difference between the two, which is the exchange splitting. The exchange splitting sharply decreases at zero electric field. This strong reduction in exchange splitting

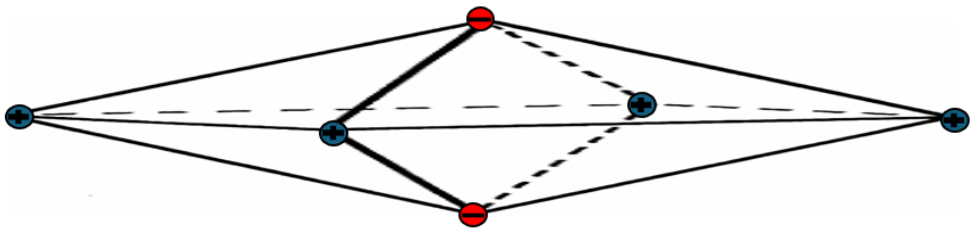

Figure 4.7: Octahedral $2e$ charged boson complex formed from two dipolar excitons and two holes. The four holes would be in a middle WSe_2 layer and the two electrons in the outer WS_2 layer, for example.

could be a signature of anti-ferroelectric correlations at zero electric field. Adjacent dipoles which are anti-aligned would only have strong exchange due to the holes in the middle layer, but aligned dipoles would have exchange due to electrons and holes; see Figure 4.6f. Thus, the reduced exchange that we observe could be a result of local anti-ferroelectric correlations of the dipolar excitons. However, this signature does not give any information about the global ordering of dipoles at zero field.

4.6 Outlook

Although there were some signatures of anti-ferroelectric correlations, the zero-field state at high density is not well-understood. An understanding of this state is interesting due to predictions of a staggered dipolar crystal. [34].

An interesting aspect of this work was the importance of dipole-dipole attraction. Given this attraction of dipolar excitons, it is natural to question the possibility of this attraction overcoming the repulsion of two electrons or holes, effectively creating a Cooper pairing mechanism. For instance, consider the complex shown in Figure 4.7. Such a structure could exist in this $WS_2/WSe_2/WS_2$ system, and possibly be a bound state. It is a $2e$ charged boson which could condense. The presence of this complex and its condensation would then make the system a light-induced superconductor.

Chapter 5

Moiré Exciton Quantum Optics

This section describes our investigation of the decay dynamics of excitons in a WS_2/WSe_2 heterobilayer. As opposed to the previous project where moiré effects are thought to be unimportant, this sample has strong evidence of the long-wavelength Moire potential creating sites for the excitons. Additionally, the on-site exciton-exciton repulsion appears to be the largest energy scale in the problem. Thus, this system can essentially be thought of as a lattice of two-level atoms with the two states being 'empty' and 'occupied.' This moiré lattice of excitons then realizes an 'array of emitters' dealt with in the literature of AMO physics and quantum optics. In AMO physics, lattices are created using the interference of light, so the spacing between atoms is of the order of the wavelength of light. However, the moiré spacing in our system is $\sim$ 8nm, two orders smaller than the wavelength of their emission light. Thus, this setting allows exploration of the deep-subwavelength regime of cooperative quantum optics.

5.1 System

The sample we consider is a WSe_2/WS_2 heterobilayer, with an optical image of the device shown in Figure 5.1b. The relative twist angle between the two layers is either 0

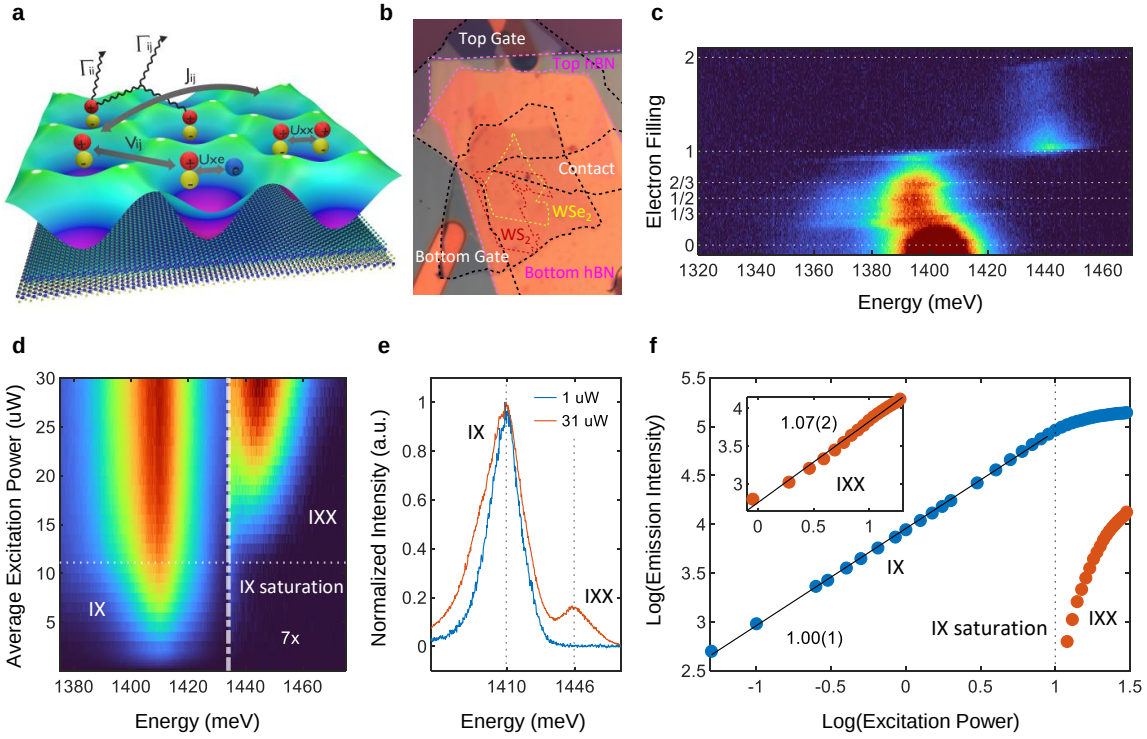

Figure 5.1: **a.** Diagram of interactions between excitons and electrons in a moiré potential in a WSe_2/WS_2 bilayer. **b.** Image of the sample. The gate scheme allows for independent application of E-field and doping. **c.** Doping scan of the photoluminescence (PL) emission of the sample, using 50nW of 740nm laser excitation. **d.** PL emission of the sample as a function of the average excitation power, using a 630nm pulsed laser. Data right of the vertical dashed line is scaled by 7x for visibility. Horizontal dashed line at 11.1 uW indicates when the IX saturates and IXX emission becomes measurable. **e.** Spectra from panel d at a low and a high excitation power, showing $U_{IXX} = 36$ meV. **f.** Intensity of the IX and IXX peaks from panel d. The intensity of IX increases linearly until the power at which IXX becomes measurable, when IX saturates. The inset shows the IXX intensity against a x-axis rescaled to the IX saturation power (log(IXX intensity) vs. log(Excitation Power - 11.1 uW)), which shows IXX intensity also increases linearly with excitation power, once the excitation power is above the saturation power.

or 60 degrees, but because of the 4% lattice mismatch between the two crystals, a moiré superlattice with peroidicity of 8nm is expected even at near-zero twist angle. [17] Figure 5.1 shows the IX PL emission as a function of the electron doping. The laser excitation is 50nW of 740nm CW. The dashed lines show sudden jumps, the first three of which we attribute to generalized Wigner crystal (GWC) states corresponding to 1/3,1/2, and 2/3 filling of the lattice with electrons, respectively. The last sudden jump occurs at complete filling of the lattice with electrons ($\nu_e = 1$), and is very large with a shift of $\sim$ 40meV. We attribute this large shift to to the presence of sites occupied by both an electron and an exciton, and denoted by U_{Xe}. Before $\nu_e = 1$, the electrons avoid the sites occupied by excitons, so this emission energy is not seen in the PL. However, after $\nu_e = 1$, it is not possible for the electrons to avoid the excitons within the spot size, so we see this emission associated with a double occupancy of an electron and an exciton.

Power dependence shows a similar phenomenon to this $\nu_e = 1$ behavior, as seen in Figure 5.1d, which shows the PL power dependence with a pulsed 640nm excitation laser. For clarity, the intensity to the right of the white dashed line is multiplied by 7. As the average power of the pulsed laser is increased from 0 to 10μW, the IX intensity increases and there is no high-energy emission. However, at approximately 11μW, a high-energy peak relative to the IX emission emerges. Line cuts of this plot at 1μW and 31μW are shown in Figure 5.1e, showing a shift of 36meV. We identify this blue peak as the emission corresponding to an exciton in a moiré site with another exciton, denoted by U_{XX}. Similarly to the doped electrons, before complete filling of the lattice with excitons, the excitons avoid each other to avoid this large on-site energy. A log-log plot of the two species' intensities versus the average excitation power is shown in Figure 5.1f. The inset shows a log-log plot for the double occupancy with the x-axis being the log of the excitation power minus 11.1μW which is the power relative to when the double occupancy first appears. We note that the double occupancy

does not have a quadratic dependence on power from zero power, the behavior we would expect without a moiré potential; it is linear starting from a minimum power. This power dependece strongly suggests that the excitons occupy sites of a moiré potential. Furthermore, we identify the average excitation power of 11.1μW with the power corresponding to complete filling of excitons, $\nu_X = 1$ within the laser's spot size. Below this power, there is at most one exciton per moiré unit cell.

5.2 An Array of Emitters

Given that below 11.1μW the excitons occupy the moiré sites and there is no double occupancy, we can model the system as an array of two level systems, with the local Hilbert space of a site being spanned by $|g\rangle$, 'ground,' meaning no exciton, and $|e\rangle$, 'excited,' meaning one exciton. In what follows we will take $\hbar = 1$. Each emitter has an energy difference between $|g\rangle$ and $|e\rangle$, denoted as ω. Furthermore, two sites can interact via an ac dipole-dipole interaction, mediated by emission of a virutal photon. For two sites i and j, the energy associated with such a process is J_{ij}, so for N sites, there is an $N \times N$ matrix corresponding to this interaction. It is conventional to assume the same resonance frequency ω for all emitters, but given that we are dealing with a solid state system, we will consider ω_i for the site i to allow for the presence of disorder. The Hamiltonian is then

$$\mathcal{H} = \sum_i \omega_i |e\rangle_i\langle e|_i + \sum_{i,j} J_{ij} |e\rangle_i\langle e|_j. \tag{5.1}$$

By defining the following operators:

$$\begin{aligned} \sigma^i_{ee} &= |e\rangle_i\langle e|_i \\ \sigma^i_{eg} &= |e\rangle_i\langle g|_i \\ \sigma^i_{ge} &= (\sigma^i_{eg})^\dagger, \end{aligned} \tag{5.2}$$

it can be written as

$$\mathcal{H} = \sum_i \omega_i \sigma^i_{ee} + \sum_{ij} J_{ij} \sigma^i_{eg} \sigma^j_{ge}. \tag{5.3}$$

This Hamiltonian, however, does not describe the decays of excitons. In reality, the excitons will be able to couple to the electromagnetic vacuum and decay from $|e\rangle$ to $|g\rangle$ via emission of a photon. It is not possible to keep track of the infinitely many vacuum modes, so these processes are modeled by considereing the time evolution of the density matrix of the array of emitters ρ, and tracing over the vacuum degrees of freedom. The result is

$$\dot{\rho} = i[\rho, \mathcal{H}] + \mathcal{L}[\rho], \tag{5.4}$$

where

$$\mathcal{L}[\rho] = \sum_{i,j} \frac{\Gamma_{ij}}{2} \left\{ 2\sigma^j_{ge} \rho \sigma^i_{eg} - \sigma^i_{eg} \sigma^j_{ge} \rho - \rho \sigma^i_{eg} \sigma^j_{ge} \right\} \tag{5.5}$$

is the Lindbladian. [35] The right two terms look like the anti-commutator $\{\rho, \sigma^i_{eg} \sigma^j_{ge}\}$, which suggests that this open system can be modeled with an effective non-Hermitian Hamiltonian

$$\mathcal{H}_{\text{eff}} = \sum_i \omega_i \sigma^i_{ee} + \sum_{i,j} \left(J_{ij} + i \frac{\Gamma_{ij}}{2} \right) \sigma^i_{eg} \sigma^j_{ge}. \tag{5.6}$$

Such an effective Hamiltonian obviously ignores the $2\sigma^j_{ge} \rho \sigma^i_{eg}$ term. However, this term can be modeled numerically by applying quantum jump operators, as is done with the Monte Carlo Wavefunction (MCWF) approach.

With this model, we recognize that our bilayer system can be described by the matrices J_{ij} and Γ_{ij} in addition to the energy scales U_{XX}, U_{Xe}, and dipole-dipole interaction V_{ij}. These energy scales are shown in Figure 5.1a. As mentioned above, the moiré setting is interesting because the spacing between 'atoms' is in the deep sub-wavelength regime, which is unattainable in AMO physics. This regime is interesting because J_{ij} and Γ_{ij} depend strongly on the ratio d/λ_0 where $\lambda_0 = 2\pi c/\omega_0$ where here ω_0 is assumed to be the frequency of all of the emitters and d is the spacing between

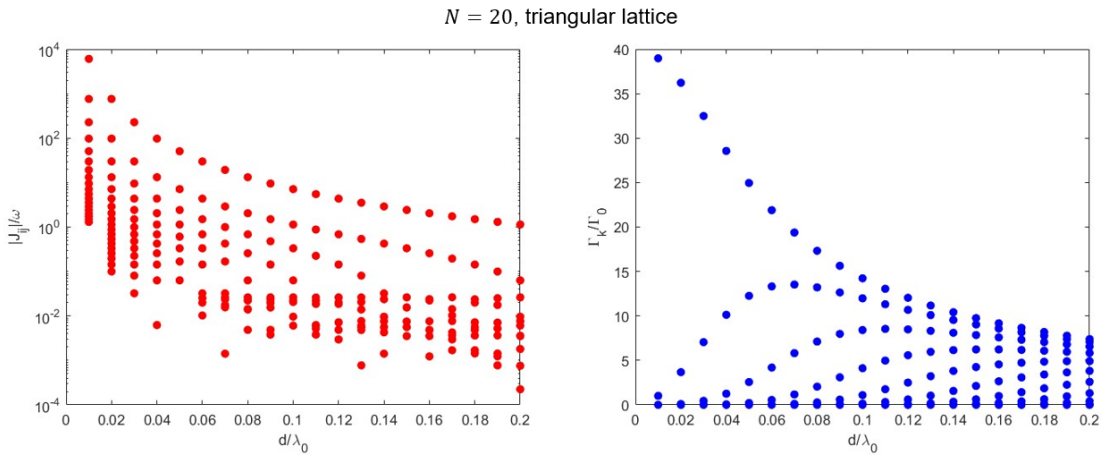

Figure 5.2: Dependence of J_{ij} and Γ_{ij} on interatomic spacing for a triangular lattice of 20 atoms. **Left:** Absolute values of elements of J_{ij} as a function of interatomic spacing d. **Right:** Eigenvalues of Γ_{ij} as a function of d in units of Γ_0.

emitters. This relationship can be observed by deriving J_{ij} and Γ_{ij} from the Green's function of the system. When the positions of the atoms do not change and all have the same resonance ω_0, the Green's function is [36]

$$\mathbf{G}(\mathbf{r},\omega_0) = \frac{e^{ik_0 r}}{4\pi k_0^2 r^3}\left[(k_0^2 r^2 + ik_0 r - 1)\mathbb{1} + (-k_0^2 r^2 - 3ik_0 r + 3)\frac{\mathbf{rr}}{r^2}\right], \tag{5.7}$$

where $k_0 = 2\pi/\lambda_0$ and $\mathbf{rr}$ is a dyadic product of $\mathbf{r}$ and $\mathbf{r}$. If $\mathbf{p}$ is the dipole moment of an emitter, then the two matrices are

$$\begin{aligned} J_{ij} &= -\omega_0^2 \mathbf{p}^* \mathrm{Re}\mathbf{G}(\mathbf{r}_i - \mathbf{r}_j, \omega_0)\mathbf{p} \\ \Gamma_{ij} &= 2\omega_0^2 \mathbf{p}^* \mathrm{Im}\mathbf{G}(\mathbf{r}_i - \mathbf{r}_j, \omega_0)\mathbf{p}. \end{aligned} \tag{5.8}$$

In the left panel of Figure 5.2, the values of J_{ij} for a triangular lattice of 20 atoms are plotted as a function of the interatomic distance d. The y-axis is log scale, so we observe that J_{ij} are much larger for smaller spacing. Furthermore, at least in the single particle picture, the eigenvalues of Γ_{ij} determine the decay rates, and the eigenvalues are plotted as a function of d in the right panel of Figure 5.2. For smaller spacing, there are much faster decay rates than at larger spacing. However, analyzing

the logarithm of these eigenvalues show that the slowest decay rates are only weak functions of the interatomic distance.

In an array of identical atoms, it has been shown that in the sub-wavelength regime for an initially incoherent half-excited lattice that there will be an initial superradiant burst followed by subradiant decay. [37] In an experimental setting, the initial superradaiance would likely deplete almost all of the excitations, so the subradiant decay would not be measurable. In our case, we are concerned with a system of excitons which is somewhat analogous to the Hamiltonian in Eq. 5.3, except that our lattice of dipolar excitons would involve the dipole-dipole interaction V. MCWF results by our collaborators Pohl et al. have demonstrated that the diagonal contribution of this dipole-dipole interaction, that is, $V_{ij}n_in_j$, can suppress superradiance, suggesting that subradiance could be measurable in a system of cooperating dipolar excitons. However, since this term is diagonal, it would not be able to realize a state with the sites having rapidly alternating phases. Superradiance results from the buildup of correlations between atoms, but subradiance is due to states with rapidly oscillating phases. However, the dipole-dipole interaction also has a long-range part, which can be written as

$$\sum_{ijkl} V_{ijkl} d_i^\dagger d_j^\dagger d_k d_l, \tag{5.9}$$

where $d_i^\dagger$ creates an exciton at site i. This term is analogous to the term describing Coulomb repulsion of electrons. Consideration of the simple case of 3 sites and 2 excitations reveals that this term could create oscillating phases on the sites. In this case, the Hilbert space is 3-dimensional, and can be written as

$$\begin{aligned} &|0,1,1\rangle \\ &|1,0,1\rangle \\ &|1,1,0\rangle, \end{aligned} \tag{5.10}$$

where 0 and 1 refer to ground and excited states, respectively. We can also assume for simplicity here that $V_{ijkl} = \tilde{V}$ is constant. It is easy to see that the matrix corresponding to the term in Eq. 5.9 using the above basis is simply

$$\tilde{V} \begin{pmatrix} 0 & 1 & 1 \\ 1 & 0 & 1 \\ 1 & 1 & 0 \end{pmatrix}. \tag{5.11}$$

By inspection clearly $(1, 1, 1)^T$ is an eigenvector with energy $2\tilde{V}$. By invoking the Perron-Frobenius theorem, this positive eigenvector corresponds to the largest eigenvalue. The physical consequence of this is that the eigenvectors which have nodes are lower energy. Thus, this term favors phases to oscillate, thus favoring subradiance.

5.3 Decay of moiré excitons in a WS_2/WSe_2 heterobilayer

Using a pulsed 640nm excitation laser, the decay dynamics of the excitons in the heterobilayer was measured. Using an avalanche photodiode, the counts as a function of time were recorded. Semi-log plots with average excitation power of less than 5μW are shown in Figure 5.3a; linear plots of the same data are in Figure 5.3d. All the plots are linear in semi-log scale, as is expected for Markovian decay. Furthemore, all of the plots, suggesting that in this range power, lifetime is independent of power. However, the behavior past 5μW is markedly different, and the semi-log plots for 5-14μW are shown in Figure 5.3b, and linear scale is shown in Figure 5.3e. Firstly, at higher powers, the counts as a function of time is linear on a linear scale for the first few hundred nanoseconds although it is expected to be an exponential since decay is assumed to be a Markovian process without any memory. Furthermore, the early time behavior clearly appears to decay slower with increased power. However, at later

times, the decay returns to an exponential for all powers with approximately the same lifetime for all powers. This late time decay is faster than the 'linear' decay observed at earlier times for the higher powers.

The decays for even higher excitation power, far past $\nu_X = 1$, is shown in Figure 5.3c. as semi-log plots, and in Figure 5.3f. on linear scale. The inset in the linear plot shows the first 50ns for 31μW, with a 'hump' attributed to the decay of doubly occupied sites into singly occupied sites, as the double occupancy wavelength has been blocked by filters. An working explanation for this slow decay is currently lacking. It could be due to cooperative effects between the excitons, as the model discussed above has Γ_{ij} eigenvalues several orders of magnitude smaller than the bare emission rate Γ_0. Thus the long-lifetime behavior could be termed as subradiance. If so, it would be, to our knowledge, the first demonstration of subradiance in a solid-state system. An issue with this cooperative quantum optics explanation lies in the fact that we do not observe any superradiance which ought to be present if indeed cooperative effects are important. However, some theoretical MCWF results done by our collaborators have indicated that the nearest-neigbor dipole-dipole interaction, V can suppress superradiant decay without interfering with subradiant decay. But generally, the theoretical MCWF results do not align well with the data, so it is quite possible that another mechanism is causing the observed behavior.

5.3.1 Time-resolved PL

Figure 5.4a. shows time-resolved PL at average pulsed laser power of 14μW. At early time, there is two peaks, with the red and blue peaks being identified with the IX and IXX emission, respectively. ν_X is barely over 1 at this power, so the IXX emission vanishes quickly with time. The IX peak is plotted as the orange dots in Figure 5.4b., and the lifetime data from an APD at this power are shown in blue. The red IX peak blueshifts with time, particularly during the long-lived 'subradiant' decay. Then,

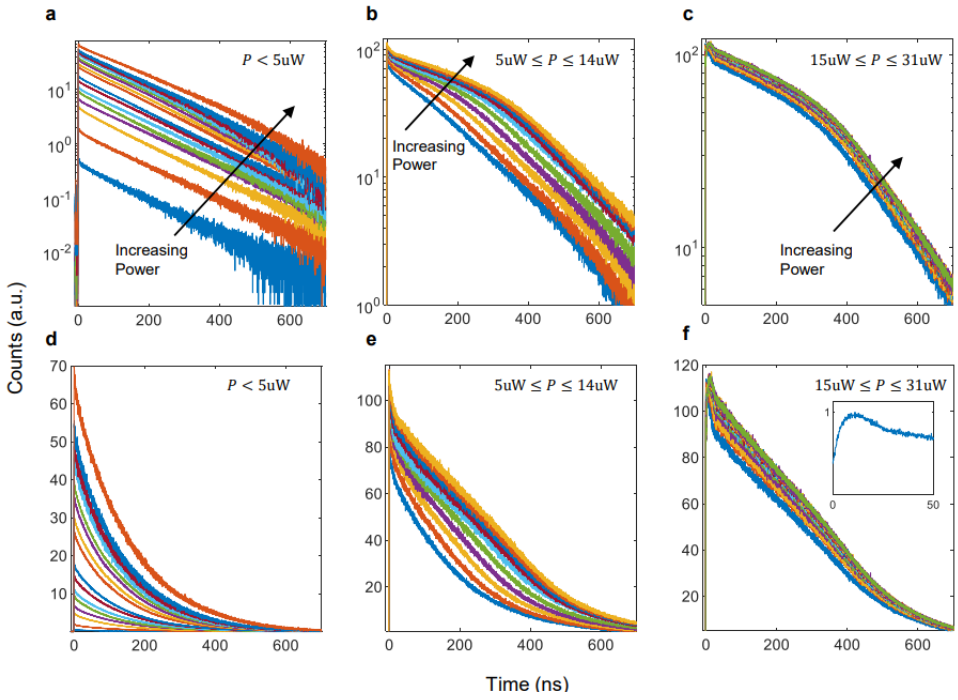

Figure 5.3: **a.** IX emission decay for the low excitation power regime (P $<$ 5 uW). The decay is exponential and lifetime is constant over the entire power range. The power for all panels of this is figure is the average excitation power, using a 630nm pulsed laser. **b.** IX emission decay for the intermediate excitation power regime (5 uW $<$ P $<$ 14 uW). The decay becomes initially linear and slower than the asymptotic decay. The transition to the slower initial regime begins at 1/2 of the IX saturation power and is fully complete at the IX saturation power. The asymptotic decay is the same as in panel a. **c.** IX emission decay for the high excitation power regime (15 uW $<$ P $<$ 31 uW). The behavior is qualitatively the same as in b, but the transition to the asymptotic behavior is progressively delayed due to the time needed for IXXs to decay to IXs. **d.** Same data as in panel a, on a linear y-axis scale. **e.** Same data as in panel b, on a linear y-axis scale. **f.** Same data as in panel c, on a linear y-axis scale. Inset shows the early-time behavior of the 31 uW decay, showing a 'hump' characteristic of the IXX to IX decay.

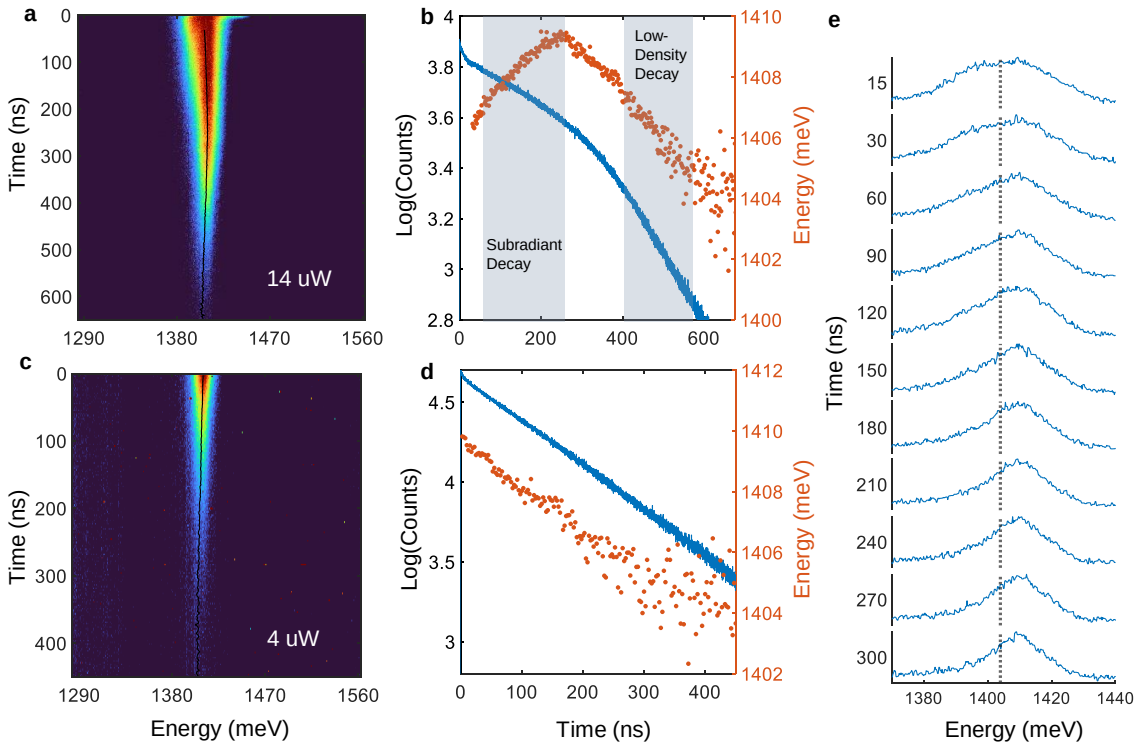

Figure 5.4: **a.** Time-resolved IX spectrum at 14μW of average excitation power, using a 640nm pulsed laser. **b.** Decay profile and extracted peak center position of the data in panel a. Note that the emission center blueshifts during the period where the decay is subradiant, and redshifts at the asymptotic, exponential period. **c.** Time-resolved IX spectrum at 4 uW of average excitation power, using a 640nm pulsed laser. **d.** Decay profile and extracted peak center position of the data in panel b. The peak redshifts, and the decay is exponential, the same behavior as the asymptotic regime of panel b. **e.** Selected lineplots of the data in panel a. The red part of the spectrum steadily disappears as the emission moves out of the subradiant regime. The dashed line indicates the asymptotic value of the IX emission, 1404 meV.

as the density continues to decrease, the peak redshifts. Different lineplots of the time-resolved PL at this power are shown in Figure 5.4e. An identical measurement at 4μW is shown in Figure 5.4c. and d. At this lower power, there is no slow decay, and there is no blueshift of the IX emission; the emission redshifts linearly with time. These redshifts and blueshifts could be an effect resulting from the significance AC dipole-dipole coupling J_{ij}, because this term causes shifts in energy between the different decay modes. However, given the lack of agreement of the data with the cooperative quantum optics model, these shifts could have a different origin. In TMD

heterobilayers, including WS_2/WSe_2, there are both optically bright and dark exciton, the latter of which do not emit light due to selection rules. These two species of excitons have different energies. There can be scattering between two optically bright excitons into two optically dark excitons, and such a process could in principle explain both the 'subradiance' and shifts. Nonetheless, even if these effects can wholly be explained by dark excitons, the behavior still depends on strong interactions between excitons, so these shifts and long lifetimes are fundamentally a many-body effect regardless of whether cooperative effects are at play.

This project is very much still ongoing, and hopefully further experiments and theoretical work will help elucidate an explanation for these observations.

Chapter 6

Conclusion

This thesis discussed two projects. The first dealt with the discovery of quadrupolar excitons in a TMD heterotrilayer. Heterobilayers host dipolar excitons, so in a heterotrilayer it would be possible for dipoles pointing either up or down out-of-plane. If interlayer tunelling is possible, then in general it would be expected that the excitons would form a superposition of 'up' and 'down' dipoles. Indeed, we found that in $WS_2/WSe_2/WS_2$ trilayers, the PL emission is starkly different from the well-known dipolar shift in heterobilayers. Rather, we observed a hyperbolic PL dispersion with electric field that only redshifts. From a simple model describing the hybridization of up and down dipoles as a two-level system, two hyperbolae are predicted, with the low-energy hyperbola corresponding to the symmetric superposition and the high-energy to the anti-symmetric. The observed PL is qualitatively similar to the low-energy branch, with the high-energy being optically dark. A more detailed consideration of the problem involved DFT calculations of the electron wavefunction for the hybridized quadrupoles, which showed that the symmetric superposition has finite electron weight in the middle WSe_2 layer where the hole is, and that this weight can be tuned by electric field. Electron-hole overlap determines the exciton lifetime, so these quadrupolar excitons have electric field-tunable light-matter coupling.

We also observed a interaction-driven quadrupole-to-dipole transition. The incident laser power allows for direct control of exciton density, and as the power was increased, the PL dependence with electric field showed dramatic qualitative changes. At low power, the sample showed a hyperbolic dispersion, but with increasing power, the dispersion, although it still only redshifted, became more and more linear, suggesting that the character of the state became more dipolar with increasing density. This effect is interaction-driven and many-body as it results from the quadrupole-quadrupole repulsion overcoming the hybridization, which is weakened as a result of phase space filling. The emission also showed strong exchange splitting which sharply decreased near zero electric field, possibly indicative of local anti-ferroelectric correlations. However, a comprehensive understanding of the zero-field state is still elusive.

The second project discussed here concerned a WS_2/WSe_2 where, in contrast to the heterotrilayer, moiré effects were of great importance. By observing PL emission associated with double occupancy of moiré sites, we recognized that this lattice was effectively an array of two-level systems, the two levels being empty or filled with an exciton, which is the system considered often in the field of quantum optics. Unlike in AMO physics, this solid state is in the deep subwavelength regime where AC dipole-dipole interactions are very strong. The time-resolved PL measurements of this system were indeed very interesting, showing anomalously long lifetimes of hundreds of nanoseconds at intermediate powers but below whole filling of the lattice with excitons. The lifetime of excitons increased with density, possibly suggesting some interaction-dependent decay dynamics. Whether or not this long lifetime decay is due to some cooperative effect is still uncertain, as it could also be explained by scattering between optically bright and dark exciton states. In any case, the effect appears to be due to exciton-exciton interactions which strongly affect the exciton decays.

In both these projects, a unifying theme is that the excitons interacted with each other. Strongly interactions between interactions can create interesting quantum

phases, but in this second project we showed that these interactions can also have fascinating consequences on their dynamics. A proper understanding of both of these projects is still lacking, and there are many more possibilities to investigate the physics of quantum phases and decay dynamics in these strongly interacting systems of dipolar excitons.

Bibliography

[1] Novoselov, K. S. *et al.* Electric field effect in atomically thin carbon films. *science* **306**, 666–669 (2004).

[2] Srivastava, A. *et al.* Optically active quantum dots in monolayer wse2. *Nature nanotechnology* **10**, 491–496 (2015).

[3] Venkata Subbaiah, Y., Saji, K. & Tiwari, A. Atomically thin mos2: a versatile nongraphene 2d material. *Advanced Functional Materials* **26**, 2046–2069 (2016).

[4] Sidler, M. *et al.* Fermi polaron-polaritons in charge-tunable atomically thin semiconductors. *Nature Physics* **13**, 255–261 (2017).

[5] Manzeli, S., Ovchinnikov, D., Pasquier, D., Yazyev, O. V. & Kis, A. 2d transition metal dichalcogenides. *Nature Reviews Materials* **2**, 1–15 (2017).

[6] Haddadi, F., Wu, Q., Kruchkov, A. J. & Yazyev, O. V. Moiré flat bands in twisted double bilayer graphene. *Nano letters* **20**, 2410–2415 (2020).

[7] Cao, Y. *et al.* Correlated insulator behaviour at half-filling in magic-angle graphene superlattices. *Nature* **556**, 80–84 (2018).

[8] Zhang, Z. *et al.* Flat bands in twisted bilayer transition metal dichalcogenides. *Nature Physics* **16**, 1093–1096 (2020).

[9] Yun, W. S., Han, S. W., Hong, S. C., Kim, I. G. & Lee, J. D. Thickness and strain effects on electronic structures of transition metal dichalcogenides: 2h-mX_2

semiconductors (m = mo, w; x = s, se, te). *Phys. Rev. B* **85**, 033305 (2012). URL https://link.aps.org/doi/10.1103/PhysRevB.85.033305.

[10] Gutiérrez, H. R. *et al.* Extraordinary room-temperature photoluminescence in triangular ws2 monolayers. *Nano Letters* **13**, 3447–3454 (2013). URL https://doi.org/10.1021/nl3026357. PMID: 23194096, https://doi.org/10.1021/nl3026357.

[11] Sammon, M. & Shklovskii, B. I. Attraction of indirect excitons in van der waals heterostructures with three semiconducting layers. *Physical Review B* **99**, 165403 (2019).

[12] Astrakharchik, G., Kurbakov, I., Sychev, D., Fedorov, A. & Lozovik, Y. E. Quantum phase transition of a two-dimensional quadrupolar system. *Physical Review B* **103**, L140101 (2021).

[13] Lozovik, Y. E., Berman, O. L. & Willander, M. Superfluidity of indirect excitons and biexcitons in coupled quantum wells and superlattices. *Journal of Physics: Condensed Matter* **14**, 12457 (2002).

[14] Dagvadorj, G., Kulczykowski, M., Szymańska, M. H. & Matuszewski, M. First-order dissipative phase transition in an exciton-polariton condensate. *Physical Review B* **104**, 165301 (2021).

[15] Cao, Y. *et al.* Unconventional superconductivity in magic-angle graphene superlattices. *Nature* **556**, 43–50 (2018).

[16] Xu, Y. *et al.* Correlated insulating states at fractional fillings of moiré superlattices. *Nature* **587**, 214–218 (2020).

[17] Regan, E. C. *et al.* Mott and generalized wigner crystal states in wse2/ws2 moiré superlattices. *Nature* **579**, 359–363 (2020).

[18] Jin, C. *et al.* Stripe phases in wse2/ws2 moiré superlattices. *Nature Materials* **20**, 940–944 (2021).

[19] Zomer, P., Guimarães, M., Brant, J., Tombros, N. & Van Wees, B. Fast pick up technique for high quality heterostructures of bilayer graphene and hexagonal boron nitride. *Applied Physics Letters* **105** (2014).

[20] Alexeev, E. M. *et al.* Resonantly hybridized excitons in moiré superlattices in van der waals heterostructures. *Nature* **567**, 81–86 (2019).

[21] Shimazaki, Y. *et al.* Strongly correlated electrons and hybrid excitons in a moiré heterostructure. *Nature* **580**, 472–477 (2020).

[22] Hsu, W.-T. *et al.* Tailoring excitonic states of van der waals bilayers through stacking configuration, band alignment, and valley spin. *Science advances* **5**, eaax7407 (2019).

[23] Li, W. *et al.* Quadrupolar–dipolar excitonic transition in a tunnel-coupled van der waals heterotrilayer. *Nature Materials* **22**, 1478–1484 (2023).

[24] Yu, L. *et al.* Observation of quadrupolar and dipolar excitons in a semiconductor heterotrilayer. *Nature materials* **22**, 1485–1491 (2023).

[25] Lian, Z. *et al.* Quadrupolar excitons and hybridized interlayer mott insulator in a trilayer moiré superlattice. *Nature communications* **14**, 4604 (2023).

[26] Barré, E., Dandu, M. & Raja, A. Quadrupolar excitons take the stage. *Nature Materials* **22**, 1437–1438 (2023).

[27] Jauregui, L. A. *et al.* Electrical control of interlayer exciton dynamics in atomically thin heterostructures. *Science* **366**, 870–875 (2019).

[28] Yu, J. *et al.* Observation of double indirect interlayer exciton in wse 2/ws 2 heterostructure. *Optics express* **28**, 13260–13268 (2020).

[29] Paradisanos, I. *et al.* Efficient phonon cascades in wse2 monolayers. *Nature communications* **12**, 538 (2021).

[30] Xiao, D., Liu, G.-B., Feng, W., Xu, X. & Yao, W. Coupled spin and valley physics in monolayers of mos 2 and other group-vi dichalcogenides. *Physical review letters* **108**, 196802 (2012).

[31] Rivera, P. *et al.* Valley-polarized exciton dynamics in a 2d semiconductor heterostructure. *Science* **351**, 688–691 (2016).

[32] Kremser, M. *et al.* Discrete interactions between a few interlayer excitons trapped at a mose2–wse2 heterointerface. *npj 2D Materials and Applications* **4**, 8 (2020).

[33] Li, W., Lu, X., Dubey, S., Devenica, L. & Srivastava, A. Dipolar interactions between localized interlayer excitons in van der waals heterostructures. *Nature materials* **19**, 624–629 (2020).

[34] Slobodkin, Y. *et al.* Quantum phase transitions of trilayer excitons in atomically thin heterostructures. *Phys. Rev. Lett.* **125**, 255301 (2020). URL `https://link.aps.org/doi/10.1103/PhysRevLett.125.255301`.

[35] Reitz, M., Sommer, C. & Genes, C. Cooperative quantum phenomena in light-matter platforms. *PRX Quantum* **3**, 010201 (2022). URL `https://link.aps.org/doi/10.1103/PRXQuantum.3.010201`.

[36] Asenjo-Garcia, A., Moreno-Cardoner, M., Albrecht, A., Kimble, H. J. & Chang, D. E. Exponential improvement in photon storage fidelities using subradiance and "selective radiance" in atomic arrays. *Phys. Rev. X* **7**, 031024 (2017). URL `https://link.aps.org/doi/10.1103/PhysRevX.7.031024`.

[37] Rubies-Bigorda, O., Ostermann, S. & Yelin, S. F. Dynamic population of

multiexcitation subradiant states in incoherently excited atomic arrays. *Physical Review A* **107**, L051701 (2023).